Materials Horizons

ROYAL SOCIETY OF CHEMISTRY

COMMUNICATION

View Article Online
View Journal

Check for updates

Cite this: DOI: 10.1039/d5mh01582k

Received 17th August 2025,
Accepted 22nd January 2026

DOI: 10.1039/d5mh01582k

rsc.li/materials-horizons

Spectroscopy-guided optimization of copper-based catalysts for low-temperature CO_2 recycling to CO

Rubén Blay-Roger, *[a] Vincent Blay, [b] Guillermo Torres Sempere,[a] Nuria García-Moncada,[ac] Tomas Ramirez Reina,[a] Bertrand Lacroix, [a] Luis F. Bobadilla[a] and José A. Odriozola [ad]

The reverse water–gas shift (RWGS) reaction provides a sustainable route for CO_2 valorization by producing CO, a key intermediate for various industrial applications. Its endothermic nature and the competition with Sabatier reaction impose a practical challenge on the design of low and medium temperature RWGS catalysts thus hampering its integration with downstream units. In this study, we investigate the design and optimization of Cu-based materials for low-temperature RWGS. A series of Cu/TiO_2 catalysts were synthesized and characterized using *operando* UV-vis, DRIFTS, and NAP-XPS spectroscopies. These studies allow us to prioritize the most promising catalyst and to derive key insights into surface intermediates, such as the formation of acrolein as a major coke precursor. These insights enable us to optimize the catalyst and mitigate deactivation through coking. Pt doping is shown to be particularly effective in reducing coke deposition, thus enhancing the long-term stability and overall catalyst's performance. Our multicomponent PtCuK@ catalyst demonstrated superior activity, selectivity, and regenerability under extended operation, opening new horizons for advanced RWGS catalysts targeting industrial CO_2 utilization. This work also provides a comprehensive framework for enhancing catalyst durability and anti-coking strategies in sustainable CO_2 valorization processes.

New concepts

We present a spectroscopy-guided strategy to develop low-temperature reverse water–gas shift (RWGS) catalysts. Unlike previous catalyst optimization studies, we use *operando* electronic and vibrational measurements to rapidly prioritize formulations. In particular, measuring electronic stability (UV-vis plasmon retention, vacancy signatures, bandgap temperature sensitivity) and surface intermediates (DRIFTS, NAP-XPS) allow us to optimize catalyst composition and architecture without lengthy reaction runs. Our resulting multicomponent catalyst (Pt–Cu–K) achieves the intended reaction mechanism, offering excellent selectivity, stability, and minimal formation of undesired acrolein-type coke precursors. This strategy may also be applicable to other redox processes where polymeric carbon deactivation limits catalyst performance.

1. Introduction

Raising atmospheric CO_2 levels are a major driver of climate change, with far-reaching impacts on society, economy, and nature.[1] Anthropogenic emissions are majorly responsible for this increase, the highest registered in the past 800 000 years.[2] Out of the 35.8 billion tons of CO_2 emitted annually,[3,4] the natural carbon cycles of Earth can only offset about half.[5] In response to this scenario, hundreds of energy policies have been deployed globally.[6] Some policies incentivize using CO_2 as a feedstock to produce valuable products.[7,8] Among these products, CO stands out as a versatile building block for the industrial synthesis of dozens of more complex molecules.[9] Although CO is mainly produced by partial oxidation or steam reforming of carbonaceous feedstocks, such as coal and natural gas, unconventional feedstocks such as biomass and pure CO_2 are also being explored. The large CO market and its strong growth projections can benefit from new production technologies.[10]

CO can be produced from CO_2 *via* direct reduction, also known as the reverse water–gas shift (RWGS) reaction.[11] This reaction is used in various industrial processes to adjust the CO_2 content of streams or to produce CO as an intermediate (*e.g.*, Fischer–Tropsch process, methanol synthesis, hydroformylation reactions and urea synthesis). Additionally, recent policies are driving the use of this reaction downstream of various combustion processes to reduce emissions, with the produced CO being utilized as a feedstock. The RWGS reaction

---

[a] Inorganic Chemistry Department and Materials Sciences Institute, University of Seville-CSIC, Sevilla, 41092, Spain. E-mail: jblay@us.es
[b] Department of Microbiology and Environmental Toxicology, University of California Santa Cruz, Santa Cruz, CA 95064, USA
[c] Servicios Generales de Investigación XPS, Centro de Investigación, Tecnología e Innovación de la Universidad de Sevilla (CITIUS), Av. Reina Mercedes 4B, 41012, Sevilla, Spain
[d] College of Environmental Science and Engineering, Beijing Forestry University, 35 Qinghua East Road, Haidian District, Beijing, 100083, P. R. China

is challenging due to the low reactivity of CO_2. The most promising low-temperature (200–500 °C) RWGS catalysts include noble metal-based catalysts and Cu-based catalysts.[11] Noble metal catalysts present high catalytic activity, but have limited selectivity and are expensive.[12] Cu-based catalysts can be very selective but tend to be less active and deactivate due to coking and sintering.[13] The Cu/ZnO–Al_2O_3 catalyst is the most widely used industrially for the forward WGS process, but it struggles with coke production when applied in the RWGS[14] and losses active copper phase above 400 °C.[15] Our group recently reported the synthesis of a Pt-based catalyst doped with Cs, which demonstrated high selectivity and activity towards RWGS.[16] Doping allowed adjusting the selectivity of Pt catalysts but their catalytic stability was compromised under reaction conditions. Wang and colleagues tackled catalyst design with machine learning, resulting in a Pt–Rb–Ba–Mo–Nb/TiO_2 catalyst.[17] The catalyst proved highly active and selective, but its synthesis is complex, and its long-term stability and recyclability were suboptimal. Nonetheless, the study showed that successful RWGS catalysts can be achieved with a balanced mix of an active base metal, a basic promoter, an electronic promoter, and a structural promoter.

In this work, we sought to develop a multicomponent catalyst to enable the conversion of CO_2 to CO with high selectivity and improved stability compared to conventional Cu-based systems. To accomplish this, we screened various copper-based materials using *operando* UV-vis spectroscopy. This allowed us to identify a promising candidate, for which we investigated its reaction mechanism using *operando* DRIFTS, NAP-XPS, and transient-pulse catalytic experiments. With these techniques, we gained insights into the formation of coke on Cu-based catalysts and hypothesized how to overcome it by rational incorporation of Pt and K, yielding a catalyst with high promise in kinetic, stability, and recyclability tests.

2. Materials

2.1. CuK@

Copper(II) nitrate trihydrate (>98%, Merck) was dissolved in deionised water (0.50 L) to give a nominal 5 wt% Cu. Under vigorous stirring (1500 rpm), 0.1 M KOH was added with a microtitration device (1 mL min^{-1}) to pH 9, and the suspension was aged at 80 °C for 12 h to form Cu precursor nanoparticles. A titanium isopropoxide solution in 2-propanol (10 vol%) was then prepared, held at 80 °C and stirred at 1500 rpm. The Cu precursor sol was fed into this solution at 100 μL s^{-1} to initiate hydrolysis and coating. After 30 min, the solid was recovered by centrifugation, washed to neutral pH, dried at 80 °C for 12 h, and calcined in air at 450 °C for 4 h (5 °C min^{-1}).

2.2. Cu(IMP)

TiO_2 support was prepared by controlled hydrolysis of a 10 vol% titanium isopropoxide solution in 2-propanol. Deionised water, used in the same total volume as in the previous synthesis, was added dropwise at 100 μL min^{-1} to promote controlled hydrolysis of the titanium precursor. The resulting suspension was aged at 80 °C under constant stirring (1500 rpm) for 12 h, then dried at 80 °C for 12 h and calcined in air at 450 °C for 4 h (5 °C min^{-1}). Subsequently, 5 g of the TiO_2 support were dispersed in 100 mL of deionised water under magnetic stirring, and copper(II) nitrate trihydrate was added in an amount calculated to achieve a nominal copper loading of 5 wt% in the final solid. The mixture was ultrasonicated for 45 min to enhance dispersion and impregnation, after which the solvent was evaporated under stirring with a rotavapor. The resulting solid was dried at 80 °C for 12 h and finally calcined in static air at 450 °C for 4 h with a heating ramp of 5 °C min^{-1}.

2.3. CuK(IMP)

TiO_2 support was prepared by controlled hydrolysis of a 10 vol% titanium isopropoxide solution in 2-propanol. Deionised water, used in the same total volume as in the previous synthesis, was added dropwise at 100 μL min^{-1} to promote controlled hydrolysis of the titanium precursor. The resulting suspension was aged at 80 °C under constant stirring (1500 rpm) for 12 h, then dried at 80 °C for 2 h and calcined in air at 450 °C for 4 h (5 °C min^{-1}). Subsequently, 5 g of the TiO_2 support were dispersed in 100 mL of deionised water under magnetic stirring, and copper(II) nitrate trihydrate was added in an amount calculated to achieve a nominal copper loading of 5 wt% in the final solid and KOH was then introduced to match the potassium loading of 10 wt% achieved in the CuK@ reference catalyst. The mixture was ultrasonicated for 45 min to enhance dispersion and impregnation, after which the solvent was evaporated under stirring. The resulting solid was dried at 80 °C for 12 h and finally calcined in static air at 450 °C for 4 h with a heating ramp of 5 °C min^{-1}.

2.4. CuK(COP)

A solution containing 10 vol% titanium isopropoxide in 2-propanol was prepared and heated to 80 °C under vigorous stirring (1500 rpm). Deionised water, previously adjusted to pH 9 with KOH and with a total aqueous volume matching that used in the preceding syntheses, was then added dropwise to the titanium solution at a rate of 100 μL min^{-1} to promote controlled hydrolysis of the titanium precursor. Once the hydrolysis step was complete, an aqueous copper nitrate solution, calculated to yield 5 wt% Cu in the final solid, was introduced dropwise at 1 mL min^{-1} into the hydrolysed Ti suspension while maintaining the temperature at 80 °C and the stirring rate at 1500 rpm. The resulting suspension was aged for 1 h at 80 °C, after which the solid was recovered by centrifugation, washed repeatedly with deionised water until neutral pH, and dried at 80 °C for 12 h. Finally, the dried solid was calcined in static air at 450 °C for 4 h using a heating ramp of 5 °C min^{-1}.

3. Methods

3.1. X-ray diffraction (XRD)

Powder X-ray diffraction (XRD) measurements were carried out on X'Pert Pro PANalytic diffractometer with Cu-Kα anode at room temperature, working at a voltage of 45 kV and a current of 40 mA. Diffractograms were registered over a 2θ range of 10°–90° with a step size of 0.05° and a step time of 300 ms.

3.2. Textural properties

The textural properties of calcined catalysts were measured by N_2 adsorption–desorption isotherms at 77 K in a Micromeritics Tristar II instrument. Prior to measurement, the samples were degassed under vacuum at 250 °C for 4 h. The specific surface area (S_{BET}) was estimated using the Brunauer–Emmett–Teller (BET) method in the relative pressure range p/p_0 from 0.05 to 0.3. The pore size distributions were estimated using the Barret–Joyner–Halenda (BJH) method.

3.3. Thermogravimetric analysis (TGA)

Thermogravimetric measurements were conducted using a TA Instruments SDT Q600 equipment under air flow (100 mL min^{-1}) and applying a temperature ramp of 10 °C min^{-1} from ambient temperature to 800 °C. All volumetric flows in this article are referred to 25 °C and 1 atm unless stated otherwise.

3.4. Temperature-programmed reduction (TPR)

H_2 temperature-programmed reduction (TPR) was performed using a U-shaped quartz reactor connected to a thermal conductivity detector (TCD). A gas flow of 50 mL min^{-1}, consisting of 5% H_2 diluted in Ar, was passed through the reactor, where approximately 75 mg of catalyst were placed. The temperature was raised up to 700 °C with a heating ramp of 10 °C min^{-1}.

3.5. Near-ambient pressure X-ray photoelectron spectroscopy (NAP-XPS)

Near ambient pressure X-ray photoelectron spectroscopy (NAP-XPS) measurements were conducted at SGI XPS in Research, Technology and Innovation Center of University of Sevilla (CITIUS). The NAP-XPS system (designed and manufactured by SPECS) was equipped with a PHOIBOS 150 NAP hemispherical energy analyzer with 1D-DLD detector, a μFOCUS monochromatic small spot X-ray source (Al Kα), a Diode Laser (976 nm) for sample heating and an *in situ* NAP cell connected to a gas mixture system to allow *operando* measurements, that is, applying the atmosphere and temperature of reaction conditions. Two samples were tested: CuK@ and PtCuK@ catalysts. Both samples were pelletized and placed in the NAP cell. Samples were subjected to ultra-high vacuum ($<10^{-7}$ mbar) at room temperature for a day before starting experiments. During experiments, a total pressure of 2 mbar was always kept, flowing either pure N_2 or a mixture of gases (H_2, CO_2, N_2). Firstly, XPS were recorded in pure N_2 flow (2 mbar in the NAP cell) at room temperature before and after a reduction step (reduction in 50% H_2/N_2 flow, at 450 °C for 1h, with a heating ramp of 10 °C min^{-1}). Then, several XPS spectra were collected under reaction conditions (also at 2 mbar in the NAP cell): 50% CO_2/H_2 at 200 and 400 °C. In all tests, high-resolution XPS spectra were collected with an energy pass of 50 eV, a step size of 0.05 eV, and a dwell time of 1s, with a small area lens opening (300 μm). The analysis and quantification of the spectra were carried out with CASA software, using Ti 2p at 458.5 eV to correct for any spectral shift due to charging.

3.6. *Operando* UV-vis experiments

Operando UV-vis experiments were carried out using a modified version of the CCR1000 reaction cell from Linkam Scientific Instruments.[18] An emission-collection probe with six radiant optical fibers and one data collection optical fiber was placed inside the reaction cell for spectroscopy. The experimental setup allows for modifying both the temperature of the reaction cell and the composition of the atmosphere. The catalyst is placed in a ceramic bed perpendicular to the radiation beam, which enables gas flow through the bed. Barium sulfate was employed as the reflectance reference for analysis. The spectral data were acquired through the averaging of 64 measurements, each taken over a 100 ms integration period. The experimental conditions for UV-vis spectroscopy were as follows: starting from an initial temperature of 25 °C, the temperature was gradually ramped up to 450 °C at a rate of 5 °C per minute, under a reducing atmosphere containing 10% H_2/Ar. Upon reaching the target temperature of 450 °C, the system was held at this temperature for 1 hour under the same conditions to ensure catalyst reduction. Following this reduction period, the gas composition was changed to 10% CO_2, 40% H_2, and 50% Ar and it was maintained at 450 °C for an additional 60 minutes. Spectra were recorded at 5-minute intervals throughout the entire process.

3.7. *Operando* DRIFTS experiments

Operando DRIFTS measurements were conducted using a Harrick HVC-DRP reaction chamber, integrated into a Praying Mantis (Harrick) DRIFTS optical system with ZnSe windows. The spectra were acquired *via* a Thermo Nicolet iS50 FTIR spectrometer equipped with an MCT detector. Background corrected spectra were collected in the range of 650–4000 cm^{-1} with a resolution of 4 cm^{-1}, averaging 128 scans for each spectrum. Gas flow was regulated using Bronkhorst mass flow controllers. Prior to each experiment, the catalyst was activated at 400 °C, with a 50 mL min^{-1} flow of 10% H_2/Ar mixture for one hour. Surface species were analyzed at five different temperatures (150, 200, 250, 300, and 350 °C), maintaining each temperature for 10 minutes and under a total flow rate of 50 mL min^{-1} (comprising 20 mL min^{-1} of H_2, 5 mL min^{-1} of CO_2, and 25 mL min^{-1} Ar). Furthermore, transient studies were conducted by alternating pulses of 50% H_2/Ar and 50% CO_2/Ar over the catalyst surface.

3.8. Transmission electron microscopy (TEM)

Transmission electron microscopy (TEM) micrographs were obtained in a JEOL 2100Plus (200 kV) with a LaB6 filament coupled with an Energy Dispersive X-ray analysis system (EDX X-Max 80 T, Oxford Instruments) and a CCD camera (Gatan) for image recording. HRTEM micrographs were obtained in a Thermo Fisher Scientific TALOS F200X equipment (200 kV) coupled to a CCD Ceta16M camera with CMOS sensor CCD. Prior to TEM and HRTEM studies, the samples were placed on a nickel support grid.

3.9. Catalytic tests

Catalytic activity was evaluated using a continuous Hastelloy X stainless steel reactor with an internal diameter of 9 mm. For each test, 200 mg of catalyst (40–60 mesh) was placed between two quartz wool plugs. Prior to reaction, the catalyst was heated *in situ* under a flow of 50 mL min^{-1} (10% H_2/90% N_2) at 10 °C min^{-1} until 450 °C and held for 1 hour. Afterwards, the temperature was lowered to the reaction temperature (*e.g.*, 250 °C) and the gas flow was changed to 60 mL min^{-1} of reaction mixture (16% CO_2/16% N_2/68% H_2). At each temperature, the products were analyzed every 30 minutes with an online Agilent 7890B gas chromatograph equipped with two packed columns (MolSieve 5A and Hayesep Q) and a TCD detector. The outlet flow rates for different components were estimated considering the response for the known flow rate of inert gas (N_2) and known response factors. Performance of the catalysts was characterized in terms of CO_2 conversion and CO selectivity, defined as follows:

$$X_{\mathrm{CO_2}} = \frac{F^0_{\mathrm{CO_2}} - F_{\mathrm{CO_2}}}{F^0_{\mathrm{CO_2}}} \tag{1}$$

$$S_{\mathrm{CO}} = \frac{F_{\mathrm{CO}}}{F^0_{\mathrm{CO_2}} - F_{\mathrm{CO_2}}} \tag{2}$$

where $F^0_{\mathrm{CO_2}}$ is the molar flow rate of CO_2 at the inlet, and F_{CO} and $F_{\mathrm{CO_2}}$ are the molar flow rates of CO and CO_2 at the outlet.

3.10. Kinetics

Kinetic parameters were estimated by assuming first order reaction kinetics between CO_2 and H_2 taking place in an ideal, isothermal plug flow reactor (PFR). In this case, the differential mass balance applied to CO_2, which is the limiting reagent, is:

$$\frac{\mathrm{d}F_{\mathrm{CO_2}}}{\mathrm{d}m} = r_{\mathrm{CO_2}} = -k(T)\cdot p_{\mathrm{CO_2}}\cdot p_{\mathrm{H_2}} \tag{3}$$

where F_j is the molar flow (mol s^{-1}) of component j (*e.g.*, CO_2), m is the catalyst mass (kg), p_j is the partial pressure of component j (Pa), r_j is the reaction rate of component j (mol kg^{-1} s^{-1}), and k is the apparent kinetic constant for the reaction (mol s^{-1} kg^{-1} Pa^{-2}) at a given temperature, T. Given the relatively small conversions studied, we neglect the effect of the reaction equilibrium in estimating the kinetic constants.

The differential mass balance can be integrated along the catalytic bed as follows:

$$m = \int_0^X \frac{F^0_{\mathrm{CO_2}}\cdot \mathrm{d}X}{k\cdot p_{\mathrm{CO_2}}\cdot p_{\mathrm{H_2}}} = \frac{F^0_{\mathrm{CO_2}}}{k\cdot\left(p^0_{\mathrm{CO_2}}\right)^2}\int_0^X \frac{\mathrm{d}X}{(1-X)(\theta-X)} \tag{4}$$

where θ is the molar ratio of H_2 to CO_2 in the reactor feed. We have also introduced the CO_2 conversion, X (eqn (1)).

We then solve the definite integral, resulting in:

$$m = \frac{Q^0}{k\cdot p^0_{\mathrm{CO_2}}\cdot R\cdot T\cdot(\theta-1)}\ln\left(\frac{\theta-X}{\theta\cdot(1-X)}\right) \tag{5}$$

Note that we have simplified terms by considering the ideal gases law:

$$F^0_j = \frac{p^0_j\cdot Q^0}{R\cdot T} \tag{6}$$

where Q^0 is the input volumetric flow (m^3 s^{-1}).

Rearranging terms further, the following equation allows estimating the apparent kinetic constant at a certain temperature given an observed conversion level, feed composition, and contact time ($\tau = m/Q^0$):

$$k = \frac{1}{\tau\cdot R\cdot T\cdot p^0_{\mathrm{CO_2}}\cdot(\theta-1)}\ln\left(\frac{\theta-X}{\theta\cdot(1-X)}\right) \tag{7}$$

The apparent kinetic constant depends on the temperature (T in K) according to the Arrhenius equation:

$$k = k_0\cdot e^{-\frac{E_a}{R\cdot T}} \tag{8}$$

where k_0 is the preexponential factor, and E_a is the apparent reaction energy.

This relationship can be linearized in an Arrhenius plot:

$$\log(k) = \log(k_0) - \frac{E_a}{R}\cdot\frac{1}{T} \tag{9}$$

4. Results

4.1. Synthesis of Cu-based catalysts

Four copper catalysts supported on titanium oxide (TiO_2) were synthesized. Titanium oxide was chosen as the support due to its redox couple (Ti^{4+}/Ti^{3+}), which enables the formation of active oxygen vacancies critical for RWGS mechanisms. For instance, compared with certain CeO_2 formulations, TiO_2 can show a more RWGS-selective response under comparable conditions, while also avoiding the handling issues of CrO_x.[19,20] Additionally, TiO_2 is more cost-effective than other redox supports with similar properties, such as CeO_2. Potassium was incorporated to suppress methanation,[21] aid in CO_2 fixation *via* the carbonate route, and encourage potassium titanate formation through alkali roasting.[22]

The Cu(IMP) and CuK(IMP) catalysts were prepared using the classical wet impregnation method, applying the precursors to TiO_2 synthesized in-house by hydrolysis.[23] The CuK(COP) catalyst was produced by mixing the co-precipitated copper and potassium with TiO_2 formed by hydrolysis. The CuK@ catalyst, in contrast, was synthesized *via* co-precipitation of copper and potassium, followed by *in situ* hydrolysis of the titanium precursor. This final approach aimed to enhance metal–support anchoring and yield a robust catalyst against ripening.[24] The compositions of the as-prepared materials are shown in Table S1.

4.2. UV-vis spectroscopy screening of potential Cu-based catalysts

Operando UV-vis spectroscopy was used to assess the electronic properties of the four Cu-based materials prepared. The formation of oxygen vacancies is key for CO_2 decomposition to CO, while the stability of the electronic spectrum provides key insights into the electronic environment when changing the gas feed.[18,25] Fig. 1 shows the changes in the intensity of the plasmon band (450–850 nm) and that of oxygen vacancies (350–400 nm) during pretreatment (450 °C, $1H_2$:$9N_2$, GHSV = 60 L g^{-1} h^{-1}) and reaction (400 °C, $4H_2$:$1CO_2$:$1N_2$, GHSV = 60 L g^{-1} h^{-1}). Table S2 quantifies the changes in areas under the curve after pretreatment and after 120 min of reaction.

The UV-vis spectroscopy results indicate that CuK@ is the most promising catalyst and it was selected for subsequent

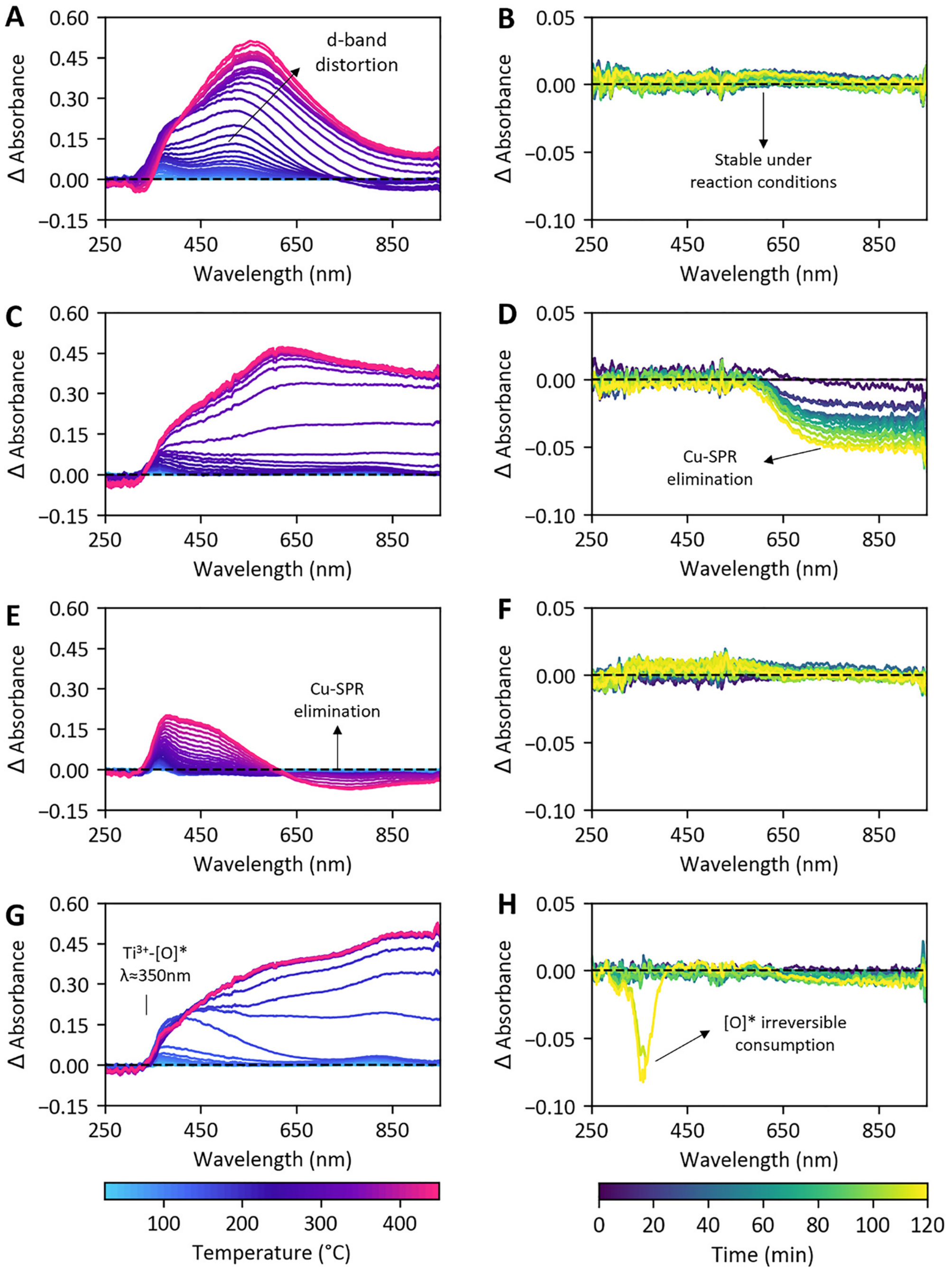

Fig. 1 UV-vis screening of materials for RWGS. Electronic spectra allowed the identification of two key properties for RWGS: oxygen vacancies and electronic stability. UV-vis results during pretreatment (T_{max} = 450 °C, 10 vol% H_2 in N_2, GHSV = 60L g^{-1} h^{-1}) and reaction (T = 400 °C, $4H_2$:$1CO_2$:$1N_2$, GHSV = 60 L g^{-1} h^{-1}). Δ Absorbance was estimated by subtracting the first normalized UV-vis spectra. (A) Difference UV-vis spectra of CuK@ catalyst during pretreatment. (B) Difference UV-vis spectra of CuK@ catalyst during reaction. (C) Difference UV-vis spectra of CuK(COP) catalyst during pretreatment. (D) Difference UV-vis spectra of CuK(COP) catalyst during reaction. (E) Difference UV-vis spectra of CuK(IMP) catalyst during pretreatment. (F) Difference UV-vis spectra of CuK(IMP) catalyst during reaction. (G) Difference UV-vis spectra of Cu(IMP) catalyst during pretreatment. (H) Difference UV-vis spectra of Cu(IMP) catalyst during reaction. Panels A, C, E, and G represent differences in the spectra with respect to the original material. Panels B, D, F, and H represent differences with respect to the activated material.

studies. More generally, the materials were ranked as follows: CuK@ > CuK(COP) > CuK(IMP) > Cu(IMP) (Table S2). CuK@ displayed an intense plasmon and the formation of abundant oxygen vacancies, which remained stable during reaction (Fig. 1A and B). The high intensity of the copper plasmon suggests the formation of small metallic clusters.[26] By contrast, the CuK(COP) and Cu(IMP) catalysts displayed variable electronic spectral stability during reaction. Specifically, CuK(COP) showed a decrease of the copper plasmon intensity (Fig. 1D), which may be associated with metal sintering, whereas Cu(IMP) exhibited an irreversible consumption of oxygen vacancies (Fig. 1H). CuK(IMP) (Fig. 1F) displayed a very weak plasmon compared to the other materials.

Besides the superior performance of CuK@ in these two criteria, the CuK@ material displayed a bathochromic shift (Fig. 1A), which we attribute to the removal of oxo ligands (O^{2-}) from the copper coordination sphere during the reduction process.[27] The resulting lower coordination is expected to decrease the local symmetry at Cu orbitals, increasing both the participation of 4p orbitals and the covalency of the electronic cloud. This electronic rearrangement should enhance the activity of Cu sites in RWGS by facilitating overlap with CO_2 antibonding orbitals.[28]

Given the expected involvement of a redox mechanism,[29] we estimated the apparent indirect electronic band gap by using the Tauc plot[30] (Fig. S1) as a qualitative descriptor of the electronic structure. This analysis revealed that the CuK(COP) catalyst had the smallest band gap among the different materials (1.61 eV) but also the lowest temperature sensitivity among all the catalysts (−0.0007 eV $^{\circ}C^{-1}$). By contrast, CuK@ exhibited a band gap of 1.78 eV, the second lowest, with comparatively high-temperature sensitivity (−0.003 eV $^{\circ}C^{-1}$). Although these values should be regarded as semi-quantitative due to the defect-rich nature of the materials, they are consistent with CuK@ displaying a more temperature-responsive electronic structure, which may facilitate redox steps during CO_2 hydrogenation.

4.3. *Operando* DRIFTS and NAP-XPS provide insights into catalyst mechanism and optimization

The CuK@ catalyst was investigated for the conversion of CO_2 to CO *via* the RWGS reaction, aiming to identify reaction pathways and key intermediates. To achieve this, *operando* DRIFTS was used to study the evolution of species on the catalyst surface. In the first experiment, the activated CuK@ catalyst was exposed to various temperatures, allowing us to observe the formation and stability of crucial intermediates during CO_2 conversion.

The DRIFTS spectra revealed a series of complex bands in 1000–1900 cm^{-1} and 2500–3100 cm^{-1} regions that required deconvolution for interpretation (Fig. 2 and Fig. S2). These bands included signals associated with carbonates and bicarbonates at 1635 cm^{-1}, 1597 cm^{-1}, 1551 cm^{-1}, 1352 cm^{-1}, 1316 cm^{-1}, and 1273 cm^{-1}, indicating that initial CO_2 activation on CuK@ occurs through the formation of carbonate species. Moreover, $\nu_{as}(CH)$ and $\nu_{s}(CH)$ bands were detected at 2930 cm^{-1} and 2835 cm^{-1}, but no bands corresponding to methyl (CH_3) groups were detected, suggesting that the mechanism involves methylene (CH_2) or vinyl species ($CH_2{=}CHR$). Strongly polarized C–H stretching bands at 2679 cm^{-1} and 2772 cm^{-1} suggest the presence of aldehydes or carboxylates, such as formates, as intermediates. These bands should be accompanied by $\delta(CH_2)$ vibrations at around 1465 cm^{-1}, which would overlap with the bands associated with carbonates and bicarbonates in this region[31] and could explain the increased intensity of the band at 1488 cm^{-1} (Fig. 2C and Fig. S2). The presence of a band at 1050 cm^{-1} can be associated with $\nu(CO)$ of simple oxygenated intermediates of the CH_xO type, bridging between formyl and methoxy species.[32] The appearance of bands at 2160 cm^{-1} and 2077 cm^{-1} suggest the coexistence of carbonyls of Cu^+ and Cu^0 respectively (Fig. S2 and S3C).[33,34]

The coexistence of the above species suggests that multiple mechanistic pathways occur simultaneously on the catalyst surface: a vacancy-mediated decomposition pathway and a Cu-centred redox pathway. In the vacancy-mediated mechanism, a Mars–van Krevelen-type route operates at the Cu–TiO_2 interface: CO_2 reacts with pre-existing oxygen vacancies of the support and lattice oxygen is cyclically removed and replenished, making the metal–support interface the critical area.[18] This interface should be at least 0.33 nm wide, corresponding to the kinetic diameter of CO_2.[35] In the redox mechanism, by contrast, CO_2 is activated and reduced on Cu^0/Cu^+ surface sites without net participation of lattice oxygen, so the relevant area is provided by the copper particles.[29,36] Fig. 2E schematically illustrates how, for sufficiently small Cu clusters, the available Cu surface and Cu–TiO_2 interfacial areas can become comparable, allowing both pathways to coexist. For larger aggregates, the redox mechanism is expected to dominate, whereas for very small clusters, the vacancy-mediated pathway would be more prevalent. HRTEM observations of the CuK@ catalyst (Fig. S16), suggest sub-nanometric Cu cluster and the absence of larger Cu aggregates, consistent with the simultaneous operation of both pathways inferred from DRIFTS.

Given that the reaction mechanism for CO_2 hydrogenation can proceed through different pathways simultaneously, we anticipated that there might be competition for metal sites during the final stage of CO formation, especially if the regeneration cycle of the metal center was not fast enough. Moreover, the convergence of different reactive intermediates near the metal center could lead to undesirable parallel reactions (*e.g.*, CH_4 formation). Indeed, the presence of formyl-like species on the catalyst are not typical intermediates during RWGS but rather during methanol formation from CO.[37]

The second experiment utilized alternating pulses of H_2/Ar and CO_2/Ar to examine how the intermediates responded to individual reactive gases. The pulse experiment (Fig. S3) confirmed that the coexistence of intermediates could result in the formation of undesired species, particularly at high CO_2 concentrations. During the CO_2 pulse, aliphatic carbonyl stretching bands at 1700 cm^{-1} and 1778 cm^{-1} were observed (Fig. S3A). These vibrations, along with the presence of methylene groups and the absence of methyl groups, suggest the formation of α,β-unsaturated carbonyl or carboxyl species (*e.g.*, acrylates or acrolein). We believe that these species could form through concerted tandem-coupling of Reppe- or Koch-type reactions with aldol.[38] The proximity of multiple highly reactive intermediates in the basic environment of the catalyst makes the production of these species possible even at 1 bar.[39,40] The absence of these species in the online mass spectrum could suggest a spectator role or poisoning effect on the catalyst. The insights from both experiments can be summarized in a mechanistic cycle (Fig. 3F).

Based on the insights gained, we hypothesized that decorating the catalyst with a low loading of platinum, due to its high spillover capacity and its ability to accommodate carbonyl groups, could improve catalytic performance. This modification could sustain various reaction pathways at the same time and enable a faster catalytic cycle. Additionally, Pt–Cu systems present singular activity in C–H and C–C bond activation,[41] we hypothesized that this modification should minimize the co-production of complex organic intermediates such as acrolein and facilitate their decomposition.[42] Based on this hypothesis, we incorporated a 0.5 wt% platinum loading onto the CuK@ catalyst, resulting in the PtCuK@ catalyst.

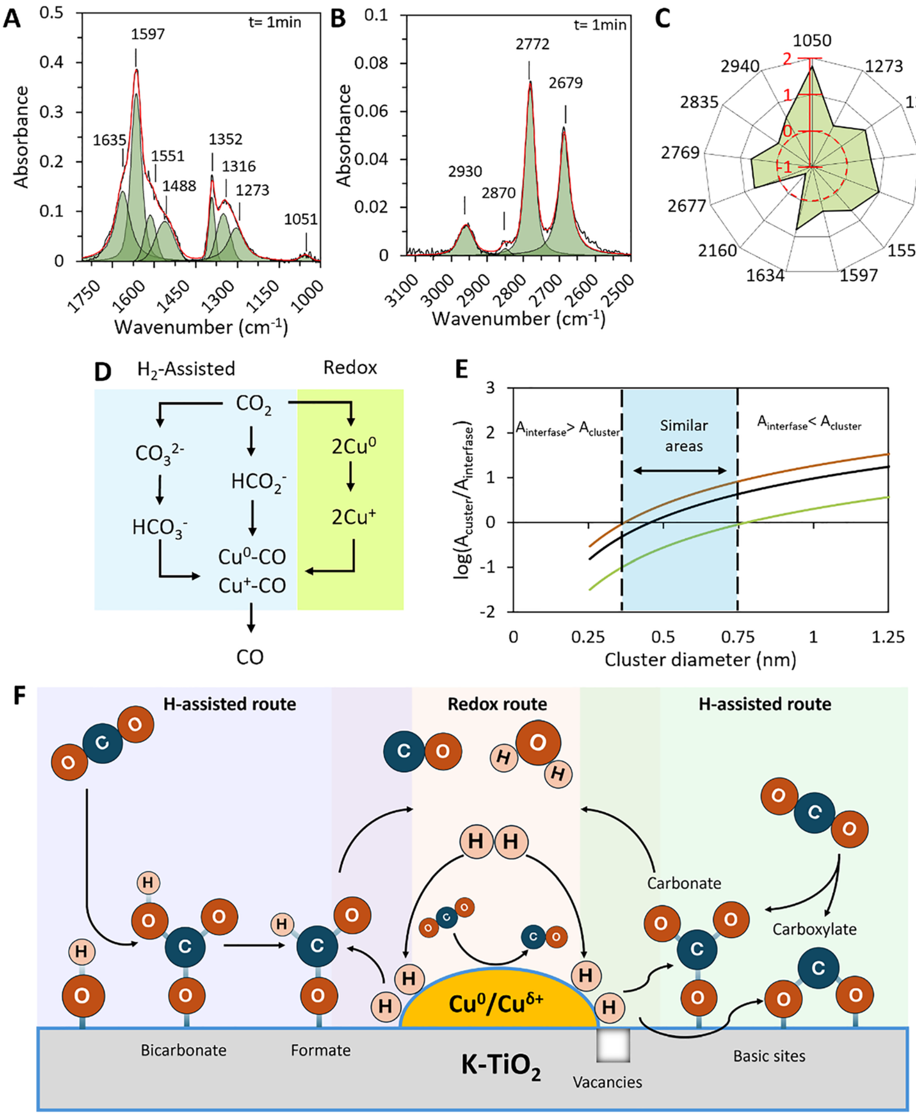

Fig. 2 Mechanistic study of catalyst CuK@. A DRIFTS experiment was conducted at T = 250 °C, $4H_2$:$1CO_2$:1Ar, GHSV = 60 L g^{-1} h^{-1}. (A) Deconvoluted DRIFTS spectrum at t = 1 min for the 1000–1900 cm^{-1} region. Black line represents experimental spectrum. Red line represents adjusted spectrum after deconvolution. (B) Deconvoluted DRIFTS spectrum at t = 1 min for the 2500–3100 cm^{-1} region. Black line represents experimental spectrum. Red line represents adjusted spectrum after deconvolution. (C) Galbraith plot showing relative band growth between t = 1 min and t = 30 min (see Fig. S2). (D) Simplified mechanism scheme for RWGS over CuK@. (E) Logarithmic relation between exposed area of metal clusters and exposed area of vacancies around metal clusters considering different hemi-cubooctahedron, hemi-icosahedron, and hemisphere. (F) Proposed catalytic mechanisms for CO_2 hydrogenation on the CuK@ catalyst. CO_2 first adsorbs on K–TiO_2 as carbonate, bicarbonate and formate, which are hydrogenated and decompose to CO in an H-assisted route on basic sites. In parallel, CO_2-derived species are reduced on $Cu^0/Cu^{\delta+}$ centres, either directly on copper or through a vacancy-mediated loop at the Cu–TiO_2 interface in which lattice oxygen is removed and replenished. The different routes are envisaged to operate concurrently, with their relative contributions set by the balance between copper surface and metal–support interface.

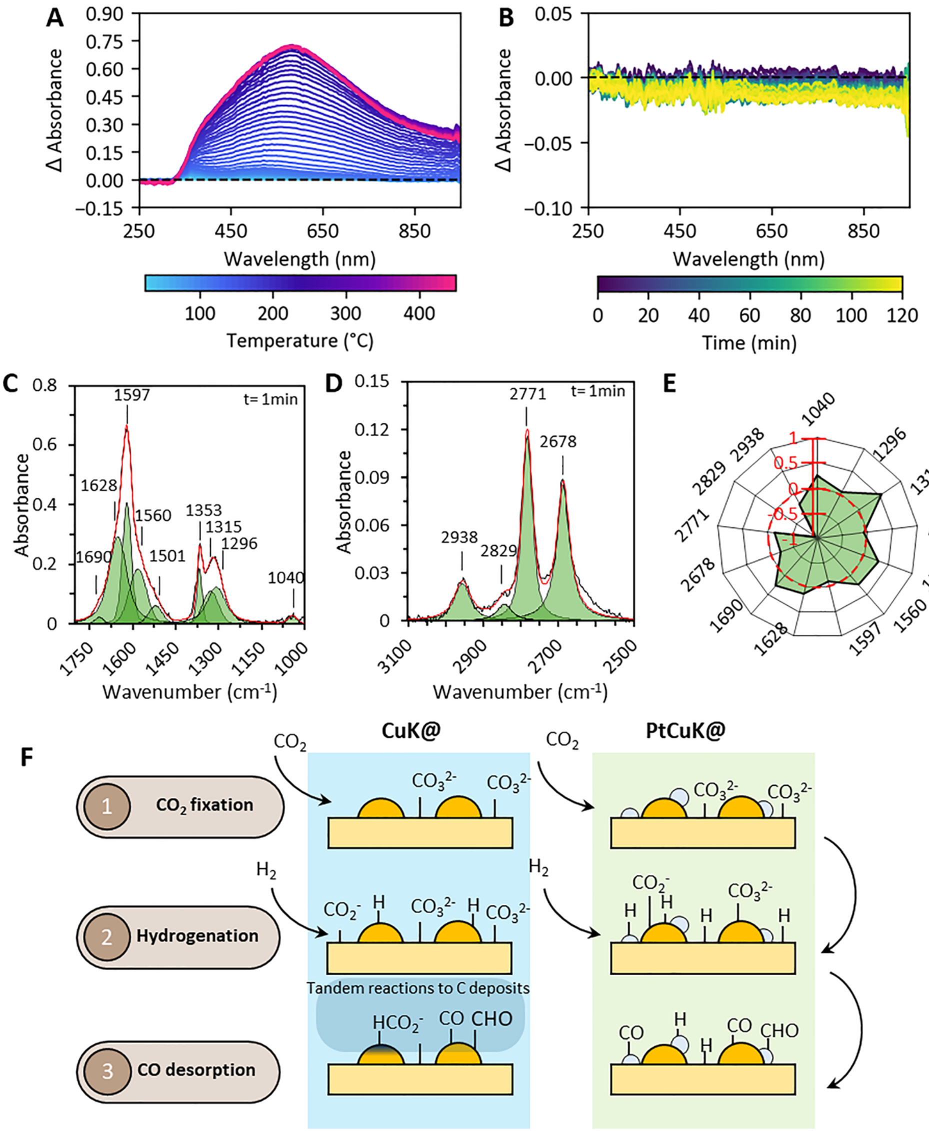

Fig. 3 Mechanistic study of catalyst PtCuK@. (A) UV-vis results during pretreatment (T_{max} = 450 °C, 10 vol% H_2 in N_2, GHSV = 60 L g^{-1} h^{-1}). Difference UV-vis spectra of PtCuK@ catalyst during pretreatment. (B) UV-vis results during reaction (T = 400 °C, $4H_2{:}1CO_2{:}1N_2$, GHSV = 60 L g^{-1} h^{-1}). Difference UV-vis spectra of PtCuK@ catalyst during reaction. (C) Deconvoluted DRIFTS spectrum at t = 1 min for the 1000–1800 cm^{-1} region. Black line represents experimental spectrum. Red line represents adjusted spectrum after deconvolution. (D) Deconvoluted DRIFTS spectrum at t = 1 min for the 2500–3100 cm^{-1} region. Black line represents experimental spectrum. Red line represents adjusted spectrum after deconvolution. (E) Galbraith plot showing relative band growth between t = 1 min and t = 30 min (see Fig. S4). (F) Proposed difference between catalytic cycles among CuK@ and PtCuK@. (1) The reaction begins with the fixation of CO_2 as carbonates and formates assisted by K. (2) Complete hydrogenation is achieved if enough H* is available on the surface. (3) CO is produced if complete hydrogenation is successful, but lack of H* may conduce to coexistence of different highly reactive and partially hydrogenated intermediates that may conduct side reactions.

The PtCuK@ catalyst was prepared and its electronic properties were examined to understand the effect introduced by the Pt decoration (Fig. 3A). The results showed an improvement in electronic properties, with an increase in the intensity of the region associated with plasmons and a decrease in the band gap (1.51 eV). The sensitivity of the band gap to temperature fluctuations was further reduced compared to the CuK@ catalyst, suggesting a more robust catalyst under varying temperature conditions. An increased intensity of the band at 350 nm indicated a higher concentration of oxygen vacancies compared to the parent catalyst. Additionally, the catalyst exhibited no changes in the electronic spectrum during 120 minutes of reaction, confirming its stability under reaction conditions. TPR experiment also showed a much lower temperature cycle compared to the parent CuK@ catalyst (Fig. S4) further evidencing the enhanced redox features for our multicomponent PtCuK@ catalyst.

Pt decoration introduced shifts in the DRIFTS band positions. The appearance of new Pt-carbonyls suggests that decoration successfully alleviates the decomposition bottleneck on the surface by introducing additional active sites.[43] Pt might also expedite CO desorption by destabilizing Cu-bound carbonyls (Fig. S5). The time-dependent blueshift of the Pt–CO bands (Fig. S5) indicates a strengthening of the CO bond at later reaction times. This could be due to a cleaning of the initial catalyst surface or to a lower electronic density over Pt atoms when alloying with less electronegative metals such as Cu, which reduces the electron backbonding from t_{2g} orbitals of Pt.[44,45] The coexistence of formate, formyl, and carbonate species confirmed the maintenance of multiple reaction mechanisms after the modification (Fig. 3B and C). However, the deconvolution of these bands over time (Fig. 3D and Fig. S6) showed a decreased accumulation of species on the catalyst compared to CuK@. This reduced accumulation evidences the role of Pt as a promoter of the different catalytic cycles. In addition, some bands lost intensity over time (Fig. 3E). Pulse experiments confirmed that the disappearance of these bands was not related to the inhibition of reaction mechanisms but to the acceleration of catalytic cycles. A comparison of the 2678 cm^{-1} bands for the CuK@ and PtCuK@ catalysts (Fig. S7A and B) showed a steeper slope for PtCuK@, confirming that the pathway remained active, and that the decomposition of the corresponding species was faster.

NAP-XPS experiments were conducted with both catalysts (Fig. S8–S12). The results confirmed the formation of complex organic species during reaction, a potential regeneration strategy, and uncommon metal synergies. In the fresh CuK@ catalyst, the Cu $2p_{3/2}$ peak at 934.4 eV with intense shake-up satellites is characteristic of surface Cu^{2+} (Fig. S8A and B). After H_2 reduction, the main Cu $2p_{3/2}$ peak shifted to 932.7 eV and the shake-up satellites were largely suppressed, while the Cu $L_3M_{4,5}M_{4,5}$ Auger line developed a new band at 918.8 eV, consistent with a mixture of Cu^0/Cu^+ at the surface. In PtCuK@, the Cu $2p_{3/2}$ binding energy was 0.3 eV lower than in CuK@, in agreement with the negative core-level shifts expected in a Pt–Cu bimetallic environment (Fig. S8C and D).[46,47] A C1s band centered at 285.2 eV (Fig. S10A and B) in both catalysts was attributed to polycarbonaceous species.[47,48] Although a reducing treatment completely suppressed this band in both systems, in the case of the PtCuK@ catalyst, this suppression was accompanied by an increase in the carbonate band at 288.9 eV. These findings suggest that the formation of these complex organic species, likely from intermediates as inferred by DRIFTS, could be reverted to their initial state with suitable regeneration of the PtCuK@ catalyst, increasing its lifetime. By contrast, their formation appears to be irreversible on the CuK@ catalyst (Fig. S9A).

4.4. Kinetic studies indicate PtCuK@ is a highly active, selective, and stable catalyst

The Cu-based catalysts were tested under typical RWGS conditions, exploring the influence of temperatures from 300 to 450 °C. In these experiments, the catalyst load (*i.e.*, 200 mg), the composition of the reactive gas (*i.e.*, 60 mL min^{-1}, $4H_2{:}1CO_2{:}1N_2$), and the residence time (*i.e.*, 360 L $g_{Cu}{}^{-1}$ h^{-1}) were fixed to compare catalytic performances.

The CO_2 conversion results from this screen are shown in Fig. 4A. The data revealed that the most active system was PtCuK@ (X = 35.7%) followed by CuK@ (X = 19.6%), both showing higher conversion than the other catalysts at temperatures above 400 °C ($X_{Cu(IMP)}$ = 1.9%, $X_{CuK(IMP)}$ = 1.9%, $X_{Cu(COP)}$ = 4.7%). At lower temperatures (<400 °C), conversion was similar among the unpromoted systems (*e.g.*, at 300 °C conversion was $X_{CuK@}$ = 1.5%, $X_{Cu(IMP)}$ = 1.4%, $X_{CuK(IMP)}$ = 0.7%, $X_{Cu(COP)}$ = 1.3%). The materials showed 100% selectivity to CO in all catalysts and conversions tested, even after Pt doping. This is already a commendable result since in this temperature range methanation is the dominant reaction.[49] We also compared the specific activities per gram of catalyst and per square meter to other Cu- and Pt-based catalysts reported in the literature under similar conversions, selectivities, and temperatures (Fig. S15 and Table S3). The comparison revealed the competitive performance of the PtCuK@ system, being superior to the Pt catalyst family in terms of activity per gram of catalyst and outperforming Cu catalysts family in terms of activity per square meter. These results also suggest that it might be possible to further boost the specific activity by increasing the area of the TiO_2 support (Table S1).

We also investigated the impact of temperature on the kinetic rates. Eqn (9) was applied to fit the apparent kinetic constant for each catalyst across different temperatures. The slope of the fitted lines provides an estimate of the apparent activation energy for the chemical transformation (Fig. 4C). The results show that the CuK@ catalyst leads to the most temperature-sensitive kinetics, with an apparent activation energy of 30 kJ mol^{-1}. Interestingly, this value is very similar to the activation energy that we previously observed for Au/TiO_2.[18] The activity of the Cu(IMP) material is very low, and it only increases slightly with temperature, with an estimated activation energy of around 3 kJ mol^{-1}, which may point to diffusional limitations. The activation energies for the CuK(IMP) and CuK(COP) are intermediate and virtually identical (*ca.* 14 kJ mol^{-1}), although the preexponential factor for the CuK(COP) is higher. This suggested that the active phase in both materials could be the same although there would be more active sites available on the CuK(COP), which is prepared by precipitation instead of impregnation.

4.5. Long reaction experiments evidence high stability and recyclability of PtCuK@

Reaction stability tests were conducted for 60 h, as shown in Fig. 4B. The PtCuK@ catalyst demonstrated higher catalytic stability compared to CuK@. The CuK@ catalyst exhibited two regimes. Initially, the conversion increased from 17.8% to 18.7% over 5 hours. This was followed by a deactivation that decelerated over time, with an average conversion loss of −0.11% h^{-1}. The PtCuK@ catalyst also showed two regimes, but it reached maximal conversion (35.7%) in a shorter time and this was followed by a much slower deactivation at −0.04% h^{-1}. The deactivation observed in CuK@ was mainly attributed to the accumulation of inactive species, as microscopy images (Fig. S16) did not reveal sintering. In the PtCuK@ system, microscopy images (Fig. S17) suggested potential Pt–Cu domain formation.[50] This interpretation is aligned with the

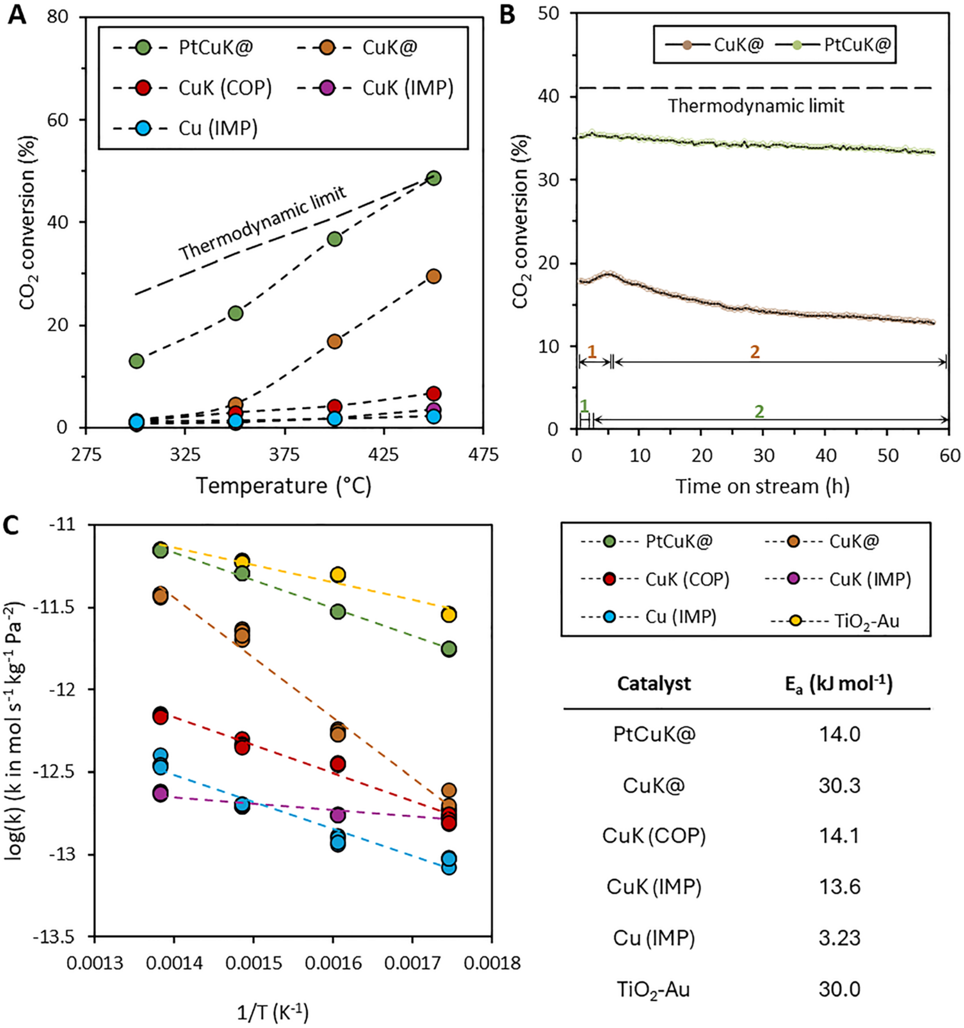

Catalyst	E_a (kJ mol^{-1})
PtCuK@	14.0
CuK@	30.3
CuK (COP)	14.1
CuK (IMP)	13.6
Cu (IMP)	3.23
TiO_2-Au	30.0

Fig. 4 Catalytic activity studies. (A) CO_2 conversion between 300 and 450 °C with GHSV = 360 L g_{Cu}^{-1} h^{-1}. The black dashed line represents the thermodynamic limit for RWGS. (B) Stability test during 60 h at 400 °C and GHSV = 300 L g_{Cu}^{-1} h^{-1} for CuK@ and PtCuK@. 1 represents the induction period until reaching the steady state. 2 represents the catalyst aging process. (C) Arrhenius plot for the different catalysts in this study, showing the dependence of the apparent kinetic constant *k* with temperature.

negative shift of the Cu $2p_{3/2}$ binding energy and the evolution of the Cu Auger band observed with NAP-XPS (Fig. S8), which indicate alloyed Cu in the reduced catalyst and a more Cu^0-enriched surface under reaction conditions. On the other hand, no carbonaceous deposits were visible under HAADF-STEM, suggesting minimal deposition. We hypothesized that the deactivation by carbonaceous species could be reversible, especially with the formation of this bimetallic alloy.[51] Thus, the regeneration of both catalysts was tested under a hydrogen atmosphere. Three types of experiments were conducted, applying a fixed regeneration time (1.5 hours) after different reaction times (1.5, 3, 15 h), which correspond to 50%, 70%, and 90% of the total operation time (Fig. S17 and Fig. 5).

The results in Fig. 5 indicate that deactivation begins early in the reaction, likely due to the formation of carbonaceous deposits on the catalyst, and these deposits appear to become more stable and harder to remove through regeneration. For the CuK@ catalyst, an 8.8% decline in activity was observed over a 15-hour period (from 17.3% at t = 0 h to 15.8% at t = 15 h). Regeneration between the first and second cycles just reversed 32% of the total activity lost. After 8 cycles and 100 hours of reaction, the activity loss ranged from 13.7% (X = 14.9%) to 16.3% (X = 14.3%). For the PtCuK@ catalyst, the activity decline over a 15-hour period was only 1.7% (from 35.3% at t = 0 h to 34.7% at t = 15 h). Regeneration between the first and second cycles restored >98% of the activity. After 100 hours of reaction and 8 cycles, the conversion loss ranged from 1.3% (X = 35.0%) to 3.5% (X = 34.2%).

These results indicate that the modification of the catalyst with platinum significantly improved its stability and recyclability. The accumulation of aliphatic species observed in DRIFTS could hinder the proper regeneration of active sites due to strong acid–base coordination. In this regard, the incorporation of Pt likely aided in the decomposition of these intermediates during the hydrogenation stage and assisted in the regeneration of nearby copper active sites (Fig. S19). *Ex situ*

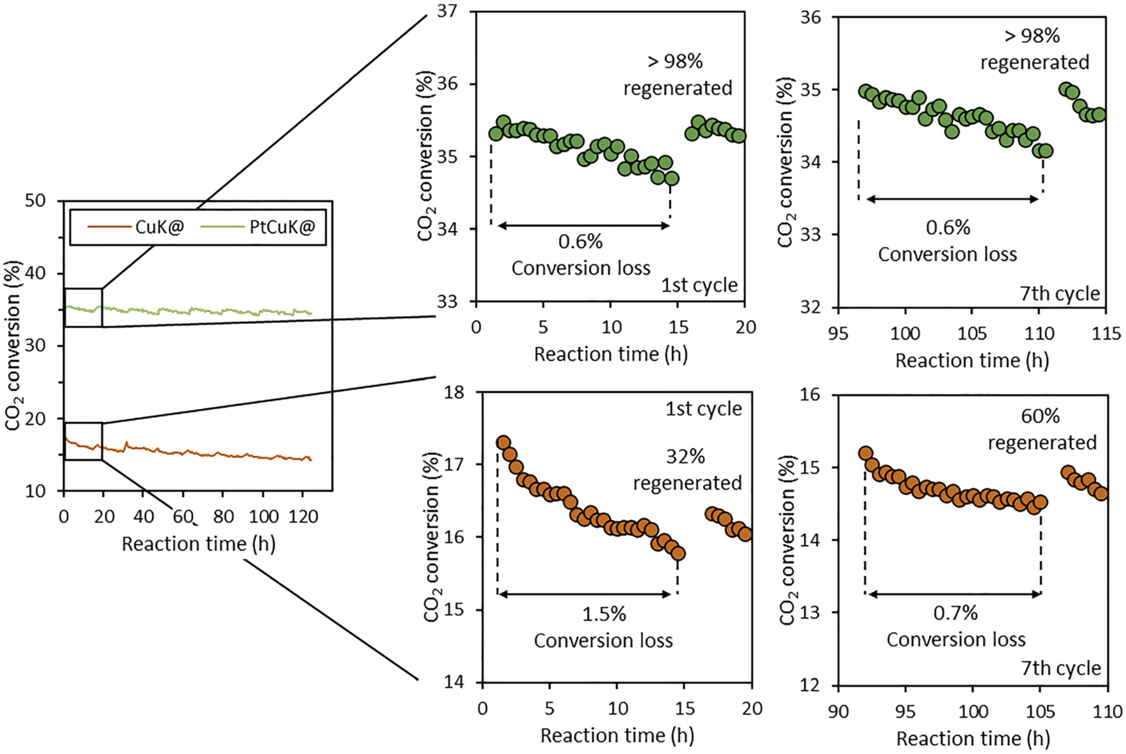

Fig. 5 Regeneration and recyclability testing. Eight long cycles were conducted each comprising 90-minutes of regeneration (1H_2:1N_2 atmosphere at 400 °C) followed by 15 hours of (T = 400 °C, GHSV = 360 L g_{Cu}^{-1} h^{-1}, H_2:CO_2 = 4).

TGA analysis of the catalysts after multiple long reaction cycles (Fig. S20) also evidenced the formation of carbonaceous deposits on the CuK@ catalyst, which were negligible on the PtCuK@ catalyst.

5. Conclusions

Despite the challenges ascribed to the design of low-temperature RWGS catalysts, this work evidences the formidable opportunities offered by multicomponent catalytic formulations. Our data demonstrates the effectiveness of the CuK@ and PtCuK@ catalysts for the selective conversion of CO_2 to CO through the RWGS reaction. The incorporation of small amounts of platinum in PtCuK@ not only increased the activity but also improved its stability and regeneration capabilities.

Operando spectroscopy and NAP-XPS studies reveal the formation of complex carbonaceous species ascribed to side reactions of intermediates. These species partially persisted over CuK@ even after regeneration but they were effectively removed from PtCuK@, suggesting differences in the reversibility of deactivation between the two catalysts. Stability tests confirmed that PtCuK@ is a promising catalyst for sustainable industrial applications in CO_2 valorization processes, such as synthetic fuel production. Indeed, our best performing catalysts showcases successful behavior for simple regeneration protocols, a highly desirable feature for realistic applications. Besides, this system works at high space velocity which allows the design of compact RWGS units saving capital cost in a potential industrial end-use. Its commendable behavior at low-temperature makes our PtCuK@ catalyst a suitable candidate for integrated RWGS-methanol synthesis or RWGS-FTS schemes providing a full cycle for CO_2 conversion to added value products. This is only possible by conducting comprehensive studies guiding the catalysts design from fundamentals to applications. Herein, our work provides a solid foundation for designing advanced catalysts that combine efficiency, stability, and regenerability for long-term use in CO_2 recycling processes.

Conflicts of interest

There are no conflicts of interest to declare.

Data availability

The data supporting this article have been included as part of the supplementary information (SI). Supplementary information is available. See DOI: https://doi.org/10.1039/d5mh01582k.

Acknowledgements

The authors acknowledge the Spanish Department of Science and Innovation (SMART-FTS, PID2021-126876OB-I00) and the Andalusian Regional Government (EMERGIA 2021, EMC21-00427) for funding, and the XPS Research Center CITIUS for the NAP-XPS utilization.

References

1 K. Rennert, F. Errickson, B. C. Prest, L. Rennels, R. G. Newell, W. Pizer, C. Kingdon, J. Wingenroth, R. Cooke, B. Parthum, D. Smith, K. Cromar, D. Diaz, F. C. Moore, U. K. Müller, R. J. Plevin, A. E. Raftery, H. Ševčíková, H. Sheets, J. H. Stock, T. Tan, M. Watson, T. E. Wong and D. Anthoff, *Nature*, 2022, **610**, 687–692.

2 D. Lüthi, M. Le Floch, B. Bereiter, T. Blunier, J.-M. Barnola, U. Siegenthaler, D. Raynaud, J. Jouzel, H. Fischer, K. Kawamura and T. F. Stocker, *Nature*, 2008, **453**, 379–382.

3 Z. Liu, Z. Deng, S. J. Davis and P. Ciais, *Nat. Rev. Earth Environ.*, 2024, **5**, 253–254.

4 World Energy Outlook 2023 – Analysis, https://www.iea.org/reports/world-energy-outlook-2023, (accessed February 11, 2024).

5 P. Friedlingstein, M. O'Sullivan, M. W. Jones, R. M. Andrew, D. C. E. Bakker, J. Hauck, P. Landschützer, C. Le Quéré, I. T. Luijkx, G. P. Peters, W. Peters, J. Pongratz, C. Schwingshackl, S. Sitch, J. G. Canadell, P. Ciais, R. B. Jackson, S. R. Alin, P. Anthoni, L. Barbero, N. R. Bates, M. Becker, N. Bellouin, B. Decharme, L. Bopp, I. B. M. Brasika, P. Cadule, M. A. Chamberlain, N. Chandra, T.-T.-T. Chau, F. Chevallier, L. P. Chini, M. Cronin, X. Dou, K. Enyo, W. Evans, S. Falk, R. A. Feely, L. Feng, D. J. Ford, T. Gasser, J. Ghattas, T. Gkritzalis, G. Grassi, L. Gregor, N. Gruber, Ö. Gürses, I. Harris, M. Hefner, J. Heinke, R. A. Houghton, G. C. Hurtt, Y. Iida, T. Ilyina, A. R. Jacobson, A. Jain, T. Jarníková, A. Jersild, F. Jiang, Z. Jin, F. Joos, E. Kato, R. F. Keeling, D. Kennedy, K. Klein Goldewijk, J. Knauer, J. I. Korsbakken, A. Körtzinger, X. Lan, N. Lefèvre, H. Li, J. Liu, Z. Liu, L. Ma, G. Marland, N. Mayot, P. C. McGuire, G. A. McKinley, G. Meyer, E. J. Morgan, D. R. Munro, S.-I. Nakaoka, Y. Niwa, K. M. O'Brien, A. Olsen, A. M. Omar, T. Ono, M. Paulsen, D. Pierrot, K. Pocock, B. Poulter, C. M. Powis, G. Rehder, L. Resplandy, E. Robertson, C. Rödenbeck, T. M. Rosan, J. Schwinger, R. Séférian, T. L. Smallman, S. M. Smith, R. Sospedra-Alfonso, Q. Sun, A. J. Sutton, C. Sweeney, S. Takao, P. P. Tans, H. Tian, B. Tilbrook, H. Tsujino, F. Tubiello, G. R. Van Der Werf, E. Van Ooijen, R. Wanninkhof, M. Watanabe, C. Wimart-Rousseau, D. Yang, X. Yang, W. Yuan, X. Yue, S. Zaehle, J. Zeng and B. Zheng, *Earth Syst. Sci. Data*, 2023, **15**, 5301–5369.

6 X. You, *Nature*, 2024, **633**, 15–16.

7 C. Hepburn, E. Adlen, J. Beddington, E. A. Carter, S. Fuss, N. Mac Dowell, J. C. Minx, P. Smith and C. K. Williams, *Nature*, 2019, **575**, 87–97.

8 T. Sakakura, J.-C. Choi and H. Yasuda, *Chem. Rev.*, 2007, **107**, 2365–2387.

9 R. M. B. Carrilho, M. J. F. Calvete, G. Mikle, L. Kollár and M. M. Pereira, *Chin. J. Chem.*, 2024, **42**, 199–221.

10 Carbon Monoxide Market Size, Share | Global Report [2032], https://www.fortunebusinessinsights.com/carbon-monoxide-market-105343, (accessed January 28, 2025).

11 H.-X. Liu, S.-Q. Li, W.-W. Wang, W.-Z. Yu, W.-J. Zhang, C. Ma and C.-J. Jia, *Nat. Commun.*, 2022, **13**, 867.

12 M. Tawalbeh, R. M. N. Javed, A. Al-Othman, F. Almomani and S. Ajith, *Environ. Technol. Innovation*, 2023, **31**, 103217.

13 Y. Choi, G. D. Sim, U. Jung, Y. Park, M. H. Youn, D. H. Chun, G. B. Rhim, K. Y. Kim and K. Y. Koo, *Chem. Eng. J.*, 2024, **492**, 152283.

14 T. Kamsuwan, A. Guntida, P. Praserthdam and B. Jongsomjit, *ACS Omega*, 2022, **7**, 25783–25797.

15 B. Liang, J. Ma, X. Su, C. Yang, H. Duan, H. Zhou, S. Deng, L. Li and Y. Huang, *Ind. Eng. Chem. Res.*, 2019, **58**, 9030–9037.

16 G. Torres-Sempere, R. Blay-Roger, L. A. Luque-Álvarez, J. L. Santos, L. F. Bobadilla, L. Pastor-Pérez, M. A. Centeno, W. Y. Hernández, I. Yousef, J. A. Odriozola and T. R. Reina, *J. Mater. Chem. A*, 2024, **12**, 1779–1792.

17 G. Wang, S. Mine, D. Chen, Y. Jing, K. W. Ting, T. Yamaguchi, M. Takao, Z. Maeno, I. Takigawa, K. Matsushita, K. Shimizu and T. Toyao, *Nat. Commun.*, 2023, **14**, 5861.

18 L. F. Bobadilla, J. L. Santos, S. Ivanova, J. A. Odriozola and A. Urakawa, *ACS Catal.*, 2018, **8**, 7455–7467.

19 Y. H. Lee, J. Y. Ahn, D. D. Nguyen, S. W. Chang, S. S. Kim and S. M. Lee, *RSC Adv.*, 2021, **11**, 17648–17657.

20 Y. Wang, L. R. Winter, J. G. Chen and B. Yan, *Green Chem.*, 2021, **23**, 249–267.

21 J. Gandara-Loe, Q. Zhang, J. J. Villora-Picó, A. Sepúlveda-Escribano, L. Pastor-Pérez and T. Ramirez Reina, *Energy Fuels*, 2022, **36**, 6362–6373.

22 S. Parirenyatwa, L. Escudero-Castejon, S. Sanchez-Segado, Y. Hara and A. Jha, *Hydrometallurgy*, 2016, **165**, 213–226.

23 S. Mahshid, M. Askari and M. S. Ghamsari, *J. Mater. Process. Technol.*, 2007, **189**, 296–300.

24 C. A. H. Price, T. R. Reina and J. Liu, *J. Energy Chem.*, 2021, **57**, 304–324.

25 J. Demuynck, M.-M. Rohmer, A. Strich and A. Veillard, *J. Chem. Phys.*, 1981, **75**, 3443–3453.

26 Y.-F. Li, F.-X. Dong, Y. Chen, X.-L. Zhang, L. Wang, Y.-G. Bi, Z.-N. Tian, Y.-F. Liu, J. Feng and H.-B. Sun, *Sci. Rep.*, 2016, **6**, 37190.

27 L. Liu and X. Chen, *Chem. Rev.*, 2014, **114**, 9890–9918.

28 M. Li, W. Hebenstreit, U. Diebold, A. M. Tyryshkin, M. K. Bowman, G. G. Dunham and M. A. Henderson, *J. Phys. Chem. B*, 2000, **104**, 4944–4950.

29 S. Fujita, *J. Catal.*, 1992, **134**, 220–225.

30 P. Makuła, M. Pacia and W. Macyk, *J. Phys. Chem. Lett.*, 2018, **9**, 6814–6817.

31 D. Lin-Vien, N. B. Colthup, W. G. Fateley and J. G. Grasselli, *The Handbook of Infrared and Raman Characteristic Frequencies of Organic Molecules*, Elsevier, 1991, pp. 9–28.

32 S. V. Ryazantsev, D. A. Tyurin and V. I. Feldman, *Spectrochim. Acta, Part A*, 2017, **187**, 39–42.

33 A. J. Maynes, D. M. Driscoll, P. A. DeSario, J. J. Pietron, A. M. Pennington, D. R. Rolison and J. R. Morris, *J. Phys. Chem. C*, 2020, **124**, 21491–21501.

34 K. Hadjiivanov and H. Knözinger, *Phys. Chem. Chem. Phys.*, 2001, **3**, 1132–1137.

35 N. Mehio, S. Dai and D. Jiang, *J. Phys. Chem. A*, 2014, **118**, 1150–1154.

36 L. Li, D. Chen, A. Anzai, N. Zhang, Y. Kang, Y. Qian, P. Du, A. Ait El Fakir, T. Toyao and K. Shimizu, *J. Catal.*, 2024, **439**, 115762.

37 N. J. Azhari, D. Erika, S. Mardiana, T. Ilmi, M. L. Gunawan, I. G. B. N. Makertihartha and G. T. M. Kadja, *Results Eng.*, 2022, **16**, 100711.

38 G. Kiss, *Chem. Rev.*, 2001, **101**, 3435–3456.

39 B. A. Sexton, A. E. Hughes and N. R. Avery, *Surf. Sci.*, 1985, **155**, 366–386.

40 S. L. Silva, T. M. Pham, A. A. Patel, S. Haq and F. M. Leibsle, *Surf. Sci.*, 2000, **452**, 79–94.

41 M. D. Marcinkowski, M. T. Darby, J. Liu, J. M. Wimble, F. R. Lucci, S. Lee, A. Michaelides, M. Flytzani-Stephanopoulos, M. Stamatakis and E. C. H. Sykes, *Nat. Chem.*, 2018, **10**, 325–332.

42 L. Chen, L. Kovarik and J. Szanyi, *ACS Catal.*, 2021, **11**, 12058–12067.

43 L. Chen, R. R. Unocic, A. S. Hoffman, J. Hong, A. H. Braga, Z. Bao, S. R. Bare and J. Szanyi, *JACS Au*, 2021, **1**, 977–986.

44 S. M. Oxford, P. L. Lee, P. J. Chupas, K. W. Chapman, M. C. Kung and H. H. Kung, *J. Phys. Chem. C*, 2010, **114**, 17085–17091.

45 L. Pasquale, S. Najafishirtari, R. Brescia, A. Scarpellini, C. Demirci, M. Colombo and L. Manna, *Chem. Mater.*, 2021, **33**, 8635–8648.

46 W. Olovsson, C. Göransson, L. V. Pourovskii, B. Johansson and I. A. Abrikosov, *Phys. Rev. B:Condens. Matter Mater. Phys.*, 2005, **72**, 064203.

47 R. Castillo, S. Navarro-Jaén, F. Romero-Sarria, V. Pérez-Dieste, C. Escudero, M. Á. Centeno, M. Daturi and J. A. Odriozola, *J. Phys. Chem. C*, 2020, **124**, 19046–19056.

48 R. Arrigo, M. Hävecker, M. E. Schuster, C. Ranjan, E. Stotz, A. Knop-Gericke and R. Schlögl, *Angew. Chem., Int. Ed.*, 2013, **52**, 11660–11664.

49 L. Yang, L. Pastor-Pérez, S. Gu, A. Sepúlveda-Escribano and T. R. Reina, *Appl. Catal., B*, 2018, **232**, 464–471.

50 V. I. Avdeev, V. I. Kovalchuk, G. M. Zhidomirov and J. L. d'Itri, *Surf. Sci.*, 2005, **583**, 46–59.

51 Z. Han, S. Li, F. Jiang, T. Wang, X. Ma and J. Gong, *Nanoscale*, 2014, **6**, 10000–10008.